Monthly Climatology of the Southern Ocean under Sea Ice

Kaihe Yamazaki [1,2], Helen Phillips [1,2,3], Maxim Nikurashin [1,2,3], Laura Herraiz-Borreguero [3,4], Paul Spence [1,2,3], Nathaniel Lee Bindoff [1,2,3]

[1]Institute of Marine and Antarctic Studies, University of Tasmania, Hobart, TAS, Australia.

[2]Australian Centre for Excellence in Antarctic Science, Hobart, TAS, Australia.

[3]Australian Antarctic Program Partnership, Institute for Marine and Antarctic Studies, Hobart, TAS, Australia.

[4]Commonwealth Scientific Industrial Research Organization, CSIRO Environment, Hobart, TAS, Australia.

Corresponding author: Kaihe Yamazaki (kaiheyamazaki@gmail.com).

Key Points:

- A multi-purpose Southern Ocean climatology including areas under sea ice is developed using a physically consistent interpolation scheme.
- The climatology outperforms other datasets in data fidelity and significantly improves thermohaline variability under the ice.
- Under-ice profiling float and biologging data prove crucial in reproducing the subpolar and continental shelf conditions, respectively.

Abstract

The advent of under-ice profiling float and biologging techniques has enabled year-round observation of the Southern Ocean and its Antarctic margin. These under-ice data are often overlooked in widely used oceanographic datasets, despite their importance in understanding the seasonality and its role in sea ice changes, bottom water formation, and glacial melt. We develop a four-dimensional climatology of the Southern Ocean (south of 40°S and above 2,000 m) using Data Interpolating Variational Analysis, which excels in multi-dimensional interpolation and consistent handling of topography and advection. The climatology captures thermohaline variability under sea ice, previously hard to obtain, and outperforms other products in data fidelity with smaller root-mean-square errors and biases. Our dataset will be instrumental for investigating seasonality and for improving ocean models. This work further highlights the quantitative significance of under-ice data in reproducing ocean conditions, advocating for their increased use to achieve a better Southern Ocean observing system.

Plain Language Summary

In the ocean close to Antarctica, measuring water temperature and salinity beneath sea ice is difficult due to the extensive ice coverage. However, it is important to develop a standard monthly-mean dataset of ocean properties under the ice to understand the ocean's seasonal cycle, which is closely related to the global climate. With the help of new tools like underwater profiling floats and marine mammals equipped with sensors, we collect ocean data throughout the year. An advanced mapping method is used to create a physically natural representation of the ocean. This new dataset provides insights that were previously hard to obtain; for example, winter ocean conditions below 100 m depth close to the Antarctic coast. The dataset will be instrumental in building our understanding of the ocean and refining our ocean models. Our results also emphasize the need for expanded use of underwater floats and biologging for a proper representation of the ocean.

1 Introduction

The Southern Ocean environment is driven by the seasonal cycle of sea ice and its extent. During winter, sea ice extensively covers the ocean around Antarctica, making it one of the most inaccessible regions globally. As a result, the seasonality of the ocean properties below the sea ice remains largely undocumented (Rintoul et al., 2010). In the past decade, our understanding of the inter- and intra-annual variability of surface circulation in the Southern Ocean has improved thanks to advances in satellite altimetry data processing that allow under-ice sea surface height to be determined (e.g., Armitage et al., 2018; Dotto et al., 2018; Mizobata et al., 2020; Auger et al.,

2021). Simultaneously, recent innovations in under-ice measurements, particularly the use of Argo floats (e.g., Klatt et al., 2007; Wong and Riser, 2011; Chamberlain et al., 2018; Oke et al., 2022) and instrumented marine mammals (e.g., Siegelman et al., 2019; McMahon et al., 2021), have facilitated ocean monitoring throughout the year. These under-ice measurements have adeptly recorded the distinct winter conditions of the Southern Ocean, specifically the surface mixed layer (Wong and Riser, 2011; Pellichero et al., 2017; Wilson et al., 2019), frontal structures (Pauthenet et al., 2021), and supercooled waters linked to sea ice formation processes (Haumann et al., 2020).

A prime example that underscores the importance of under-ice data is the subsurface seasonality of the Southern Ocean. This significantly affects stratification at the base of the mixed layer and the penetration of warm subsurface waters into the mixed layer, thereby influencing sea ice extent across interseasonal timescales (Wilson et al., 2019; Doddridge et al., 2021; Libera et al., 2022). The freshwater flux mediated by sea ice plays a fundamental role in the upper branch of the meridional overturning circulation (Abernathey et al., 2016; Haumann et al., 2016; Pellichero et al., 2018). Furthermore, our understanding of the long-term trends in Antarctic and Southern Ocean water masses has primarily been derived from summer data (Schmidtko et al., 2014; Yamazaki et al., 2021; Herraiz-Borreguero and Naveira Garabato, 2022). Atmospheric trends over the Southern Ocean have a distinct seasonal asymmetry, such as the summer-biased strengthening of the Southern Annular Mode (Hazel et al., 2019; Neme et al., 2022; Fraser and Wongpan et al., 2023). The seasonally asymmetric trends are likely key in triggering the climatic regime shift in the Southern Ocean and Antarctica (Herraiz-Borreguero and Naveira Garabato, 2022; Purich and Doddridge, 2023; King et al., 2023). These factors

motivate the need for a standard monthly climatology of the Southern Ocean interior that extends beneath the sea ice.

The task of curating and analyzing under-ice data currently poses significant challenges for a large portion of the scientific community. Consequently, this barrier can lead to misrepresentation in ocean models and thus inaccurate predictions for changes in climate and sea level. One critical reason for the underutilization of under-ice Argo float is the absence of position information. Position data are only available when floats surface in ice-free ocean areas. Under sea ice, float positions are inferred by interpolating between two surface locations in a straight line or along a dynamically-consistent path, in which positional errors are typically around 50 km (Chamberlain et al., 2018; Yamazaki et al., 2020; Oke et al., 2022). Around 40% of the Argo profiles collected in the Southern Ocean seasonal ice zone are flagged as under ice (Yamazaki et al., 2020). The Argo float constitutes the most significant portion of profile numbers in the ocean interior, while biologging data dominate the profile numbers near the Antarctic margin (e.g., Pauthenet et al., 2021). Despite the abundance of the under-ice profiles in the Southern Ocean, they have not been included in major datasets such as the NOAA World Ocean Database (https://www.ncei.noaa.gov) and the Hadley Centre EN4 (https://www.metoffice.gov.uk/), which are commonly used for initializing climate models. No existing climatology product includes both under-ice Argo and biologging data except in specific applications for physical oceanography investigations (e.g., Pellichero et al., 2017; Pauthenet et al., 2021). This is despite increasing demands for these data to be used in high-resolution ocean modelling and ocean biogeochemistry studies at the Antarctic margin.

In this study, we develop a novel four-dimensional monthly climatology of the Southern Ocean that includes the under-ice data. Historically, various methods have been employed to

map oceanographic properties in the Southern Ocean, such as optimal interpolation with topographic constraints (Ridgway et al., 2002; Shimada et al., 2017; Mensah and Ohshima, 2023), fast-marching algorithm (Schmidtko et al., 2013; 2014), and several machine learning techniques (Giglio et al., 2018; Yamazaki et al., 2020; Pauthenet et al., 2021; Sonnewald et al., 2023). The present study adopts the Data Interpolating Variational Analysis (DIVA; Barth et al., 2014; Roach and Bindoff, 2023), which offers enhanced capabilities in handling topographic and advection constraints, multi-dimensional interpolation (including time), and superior statistical performance compared to conventional methods (see Section 2.2 and Text S1 for details). Our analysis incorporates both under-ice Argo and biologging data as performed in Pauthenet et al. (2021), but extends northward to 40°S and downward to 2,000 dbar with a finer horizontal resolution. We juxtapose our results with the latest version of World Ocean Atlas (WOA23; Regan et al., 2023; Locarnini et al., 2023) and the Southern Ocean State Estimate integrated with biogeochemical components (B-SOSE; Verdy and Mazloff, 2017). The B-SOSE solution is eddy-permitting and adjusted to observations by tuning model parameters and boundary conditions.

This paper is structured as follows: Section 2 details the data and methods used for the monthly climatology with the DIVA interpolation. Section 3 presents the interpolated climatology and compares it to the other datasets. Section 4 provides the conclusions. In this paper, we present a succinct overview of the subsurface seasonality. Given its relevance to a broad spectrum of scientific interests and perspectives, it warrants more extensive investigation.

2 Data and Methods

123 2.1 Input data

124 Conductivity-Temperature-Depth (CTD) profiles from multiple instrument types are
125 collected: the Argo float (Argo, 2000; Wong et al., 2020), biologging data from instrumented
126 seals (MEOP; Roquet et al., 2021; McMahon et al., 2021), and ship-based measurements
127 available in the World Ocean Database (Boyer et al., 2018). The collected observations are
128 overviewed in Figure 1a and 1b. The treatment for the quality flags and the under-ice Argo data
129 is noted in Text S2. The collected profiles span the period from 1910 to 2023. As shown by
130 Pauthenet et al. (2021), there is a notable observation density bias toward the period post-2005,
131 primarily due to the prevalence of Argo and biologging profiles. Consequently, the resulting
132 climatology is predominantly representative of this recent timeframe. From the CTD profiles, we
133 extract surface data for temperature and salinity across the interpolating layers using Akima
134 interpolation at 1 m intervals.

135 The additional input data for DIVA are outlined in Figure S1. The International
136 Bathymetric Chart of the Southern Ocean, version 2 (IBCSOv2; Dorschel et al., 2022), provides
137 the topographic constraint. The horizontal correlation scale is proportionally aligned with the
138 bathymetric gradient, which is then mapped onto the interpolation grid. For the advection
139 constraint, we use the climatological velocity from B-SOSE iteration 136 (Figure S2a). An
140 assessment of this advection constraint can be found in Text S5. The background field for DIVA
141 temperature and salinity is derived from the climatological field of WOA23. This implies that the
142 temporal variation in the derived field (e.g., Figure S9a) is based solely on the collected CTD
143 profiles, while the spatial variation is somewhat influenced by WOA23. Further details about the
144 input data are provided in Text S2.

2.2 Data Interpolating Variational Analysis

We employ the multidimensional DIVA implemented by a Julia package DIVAnd (Barth et al., 2014), which facilitates the semi-automatic calibration of tuning parameters. As in Roach and Bindoff (2023), we perform three-dimensional DIVA in horizontal/time dimensions and iterate the process across vertical layers to construct the four-dimensional climatology. In the version of the climatology released with this paper (2023.11), the dataset covers 66 layers ranging from 5 to 2,000 m, following the standard levels of WOA23. The interpolation grids are circumpolar between 75°S to 40°S with grid intervals set at 1/2° in longitude, 1/4° in latitude and monthly in time. This horizontal grid configuration results in an approximate 25 km interval at 60°S, which appears adequate to smoothly capture the synoptic-scale variability (e.g., Auger et al., 2022).

To optimize the analysis for the Antarctic margin, interpolation tests are conducted south of 50°S (detailed in Text S3). Based on these tests, we determine the relative correlation time scale and advection weighting (see also Figure S1). Simultaneously, the correlation scaling factor and smoothing factor (signal-to-noise ratio) are automatically calibrated using the cross-validation function (Troupin et al., 2012), which aims to minimize data residuals and interpolation biases. By multiplying the relative correlation scales in space and time with the correlation scaling factor, we determined the correlation time scale to be 1.86 months, and the horizontal correlation scale to range between 100 and 400 km (see Figure S2). This calibrated correlation scale broadly aligns with findings from previous studies on optimal interpolation (Shimada et al., 2017) and model analysis (Mazloff et al., 2018; Auger et al., 2022).

The interpolation error linked with DIVA is estimated using the approximation method in Beckers et al. (2014), a feature integrated into the DIVAnd package. This interpolation error tends to escalate in areas where data is sparser, both spatially and temporally (Figure 1d). As detailed in Text S4, potential error associated with spatial smoothing due to the nonlinear nature of the equation of state (known as cabbeling) can be crudely corrected using the standard deviation of temperature and salinity following the method in Schmidtko et al. (2013). More information about the procedure of DIVA can be found in Supporting Information.

3 Results

3.1 Interpolated field

In Figure 1, the data distribution by platform, observed temperature at 100 m, and the DIVA-interpolated temperature are presented for March, June, September, and December. The DIVA field accurately reproduces the nuances of the original observations, as illustrated in Figures 1b and 1c. Interpolation error can become significantly large over the continental shelf due to data scarcity (Figure 1d), so that areas with an interpolation error over 1°C have been masked out in Figure 1c. Conversely, areas with abundant data exhibit small interpolation errors. In these regions, a large standard deviation indicates substantial spatiotemporal variation, likely corresponding to significant horizontal gradients in temperature or salinity. The DIVA field and observational data are further compared in time series in Figure S5, demonstrating how the sparsity and dispersion of observations relate to the interpolation error and standard deviation. Both variables serve as statistical measures for assessing the DIVA interpolation. As depicted in Figure S9a, the DIVA field captures the widespread seasonal variation of the 100 m temperature

by up to 1°C, which has not necessarily been evident in other datasets. Monthly maps of the interpolated temperature and salinity from 5 to 2,000 m are available in Movie S1.

As a result of the semi-automatic calibration of the tuning parameters, the misfit of the DIVA field from observations is very small. South of 60°S (i.e., the southern part of the interpolation test domain; Section 2.2), the root-mean-square error of annual mean potential temperature at 100 m is estimated to be 0.492°C, and the bias is less than 0.000°C. For salinity at 100 m, the root-mean-square error is 0.089 psu, and the bias is less than 0.000 psu. Crucially, these statistics outperform those of WOA23 and the B-SOSE monthly climatology as shown in Section 3.2).

3.2 Comparison with other datasets

Figure 2 compares the DIVA temperature at 100 m in March and September with the corresponding data from WOA23, which does not include biologging data, and with the monthly climatology derived from the B-SOSE iteration 136. The B-SOSE solution spans from 2013 to 2021. Constructing the DIVA using observations over the same period shows that the difference in time period does not affect the following comparison. In Figure 2, areas with large interpolation error are not masked, since the corresponding error estimate — expected to be larger in areas with sparse observations — is unavailable in both WOA23 and B-SOSE.

DIVA and WOA23 are consistent on the basin-scale temperature variations (Figures 2a and 2b), while noticeable differences in nuances are observed on smaller scales. Generally, DIVA is smoother than WOA23. For instance, in September, WOA23 depicts warm blobs crossing the continental slopes (indicated by black arrows) and forming spotty patterns offshore (indicated by a white arrow). Despite the potential for spurious interpolation due to data scarcity

during the freezing season, DIVA successfully derives a physically consistent field. Meanwhile, the B-SOSE temperature is significantly warmer than the DIVA field in both March and September (by around 1°C; see also Figure S8), indicating relatively large biases in the model solution.

In WOA23 and B-SOSE, the misfit from the observations is generally larger than that for the DIVA product. South of 60°S, the root-mean-square error increases to 0.587°C for WOA23 and 1.307°C for B-SOSE, and the bias increases to -0.013°C and 0.657°C, respectively (Figure 2d). The data fidelity of DIVA is further highlighted when focusing on specific periods or areas with a limited number of data points, such as in September (Figure 2e) and on the continental shelf (Figure 2f). In these cases, the root-mean-square error/bias differences from DIVA to the two datasets become more pronounced than in the annual mean south of 60°S (Figure 2d). A similar discussion can be derived from the comparison in salinity at 100 m (Figure S7).

The vertical structure is summarised in zonally-averaged meridional sections (Figure 3). The standard deviation of temperature and salinity, indicative of the strength of seasonal variation, demonstrates surface-originated seasonality in all datasets. The penetration of this seasonality is typically characterised by the extent of winter water below 0°C. WOA23 exhibits a zonally-averaged structure similar to that of DIVA, but has less smoothed features (Figure 2b, arrows) that result in greater subsurface seasonal variation than in DIVA (Figures 3a, 3b and 3d). The 100 m temperature difference from DIVA (Figure S8b) and the difference in the monthly temperature anomalies (Figures S9a and S9b) are also related to this discrepancy.

The seasonality of B-SOSE does not extend as deeply as in the DIVA field (Figures 3a, 3c), and the difference in the annual-mean temperature (Figure 3e, top panel) shows a positive

peak around 100 m that connects to deeper layers in the north where B-SOSE is much warmer than DIVA. The salinity plots are largely a mirror image of temperature, with B-SOSE being much fresher than DIVA toward the surface. The B-SOSE and the DIVA fields have relatively good agreement in near-surface temperature. The discrepancy in subsurface temperature is thus likely related to the modeled mixed layer depth and winter water. The reason for this misrepresentation could be linked to the near-surface fresh bias. The fresh surface layer can act as a barrier to surface mixing, leading to shallow winter convection and warm bias at depth. The DIVA climatology and the presented datasets are further assessed in Text S5.

3.3 Effect of including under-ice data

To quantify the importance of under-ice data, two additional DIVA fields are constructed, one excluding under-ice Argo data ("no-iceArgo") and the other excluding biologging data ("no-MEOP"). Their temperature differences compared to the referential DIVA at 100 m are shown in Figure 4, characterising the effect of including these data in capturing the seasonality. Inclusion of the under-ice Argo data results in changes in the DIVA temperature by ~1°C in June and September, while also significantly reducing the interpolation error by more than 1°C (Figures 4a and 4b). This effect stands out clearly along the Antarctic margin, between the climatological sea ice extent maxima and the continental slope isobath.

In contrast, the inclusion of biologging data has a noticeable effect over the continental shelf (Figures 4c and 4d). There, its influence on the DIVA temperature and the interpolation error is found to be comparable in magnitude to the influence of the under-ice Argo data. Although this effect may be relevant to the observed differences between the reference DIVA and WOA23 (Figure S8b), as the latter does not include the biologging data, there is no clear

correlation. The significant impacts of incorporating under-ice Argo data and biologging data in the different areas highlight their irreplaceable roles in reproducing the seasonality of the Southern Ocean and the oceanic conditions under sea ice.

4 Conclusions

Historically, under-ice measurements in the Southern Ocean have been hindered by the extensive presence of sea ice. Under the current climate of rapid change in the ocean and ice around Antarctica, it is crucial to have a monthly climatology that covers beneath the sea ice to answer questions related to the seasonal variability (e.g., of air-sea-ice interaction and ocean heat transport). However, no multi-purpose monthly climatology focusing on the under-ice Southern Ocean has been made due to the challenges in curating and combining under-ice data from various platforms. This barrier to under-ice data observations has been a significant obstacle in assessing performance of ocean models particularly during the freezing season, potentially leading to inaccurate climate predictions.

In this study, we have developed a monthly climatology of the Southern Ocean that incorporates both under-ice Argo and biologging data. We used the DIVA scheme, an advanced type of conventional optimal interpolation that enables a relatively simple multi-dimensional interpolation and handling of topographic and advection constraints. By maintaining physical consistency and data fidelity, our climatology successfully captures the subsurface seasonality more accurately, a feature previously challenging to reproduce in other climatologies and state estimate simulations. Furthermore, the comparison between the referential climatology and the climatology excluding under-ice data revealed that the inclusion of under-ice data alters the 100-m temperature by approximately 1°C and decreases the interpolation error by more than 1°C.

The under-ice Argo data are crucial for accurately representing the subpolar Southern Ocean during winter, and the biologging data are essential for accurately representing ocean conditions over the continental shelf. This result represents the first quantification of the effect of under-ice data on constructing a climatological dataset.

Our results underscore the critical need for expanding the use of both under-ice Argo floats and biologging techniques to improve monitoring of the Southern Ocean. Argo is currently adapting its global coverage plan to include polar regions and marginal seas (as part of Polar Argo), areas that were initially excluded from the original design due to technological constraints. In conjunction with ship-based measurements, which will remain an essential observation platform in the Antarctic margin heavily covered by sea ice, these autonomous observation techniques provide unique and complementary contributions to the complete coverage. The integration of these different platforms is expected to occur through close communication via the Southern Ocean Observing System (SOOS; Rintoul et al., 2010; Newman et al., 2019) and the Global Ocean Observing System (GOOS).

Acknowledgments

We thank Christopher Roach and Matthias Auger for valuable comments. This research was supported by the Australian Research Council Special Research Initiative, Australian Centre for Excellence in Antarctic Science (Project Number SR200100008) and by the Australian Government as part of the Antarctic Science Collaboration Initiative. Computational resources for the SOSE were provided by NSF XSEDE resource grant OCE130007 and NSF award PLR-1425989. Among contributions to the International Argo Program by several countries and programs, we especially thank the SOCCOM program.

Open Research

The Southern Ocean monthly climatology presented in this study is open to the public via Zenodo (https://doi.org/10.5281/zenodo.10350472). The Argo data were collected and made freely available by the International Argo Program (http://www.argo.ucsd.edu, https://www.euro-argo.eu). The biologging data were made freely available by the International MEOP Consortium and the AniBOS network (http://www.meop.net). World Ocean Database and World Ocean Atlas are available from National Centers for Environmental Information, NOAA (https://www.ncei.noaa.gov). B-SOSE solutions are publicly available from University of California, San Diego (http://sose.ucsd.edu). Julia package DIVAnd is accessible via GitHub (https://github.com/gher-uliege/DIVAnd.jl).

References

1. Abernathey, R. P., Cerovecki, I., Holland, P. R., Newsom, E., Mazloff, M., & Talley, L. D. (2016). Water-mass transformation by sea ice in the upper branch of the Southern Ocean overturning. Nature Geoscience, 9(8), 596-601.
2. Argo (2000). Argo float data and metadata from Global Data Assembly Centre (Argo GDAC). SEANOE. https://doi.org/10.17882/42182
3. Armitage, T. W., Kwok, R., Thompson, A. F., & Cunningham, G. (2018). Dynamic topography and sea level anomalies of the Southern Ocean: Variability and teleconnections. Journal of Geophysical Research: Oceans, 123(1), 613-630.
4. Auger, M., Prandi, P., & Sallée, J. B. (2022). Southern ocean sea level anomaly in the sea ice-covered sector from multimission satellite observations. Scientific Data, 9(1), 70.
5. Barth, A., Beckers, J. M., Troupin, C., Alvera-Azcárate, A., & Vandenbulcke, L. (2014). divand-1.0: n-dimensional variational data analysis for ocean observations. Geoscientific Model Development, 7(1), 225-241.

6. Beckers, J. M., Barth, A., Troupin, C., & Alvera-Azcárate, A. (2014). Approximate and efficient methods to assess error fields in spatial gridding with data interpolating variational analysis (DIVA). Journal of Atmospheric and Oceanic Technology, 31(2), 515-530.
7. Boyer, T.P., Baranova, O.K., Coleman, C., Garcia, H.E., Grodsky, A., Locarnini, R.A., Mishonov, A.V., Paver, C.R., Reagan, J.R., Seidov, D., Smolyar, I.V., Weathers, K., & Zweng, M.M. (2018). World Ocean Database 2018. In A.V. Mishonov (Tech. Ed.), NOAA Atlas NESDIS 87.
8. Chamberlain, P. M., Talley, L. D., Mazloff, M. R., Riser, S. C., Speer, K., Gray, A. R., & Schwartzman, A. (2018). Observing the ice-covered Weddell Gyre with profiling floats: Position uncertainties and correlation statistics. Journal of Geophysical Research: Oceans, 123(11), 8383-8410.
9. Doddridge, E. W., Marshall, J., Song, H., Campin, J. M., & Kelley, M. (2021). Southern Ocean heat storage, reemergence, and winter sea ice decline induced by summertime winds. Journal of Climate, 34(4), 1403-1415.
10. Dorschel, B., Hehemann, L., Viquerat, S., Warnke, F., Dreutter, S., Tenberge, Y. S., ... & Arndt, J. E. (2022). The international bathymetric chart of the southern ocean version 2. Scientific data, 9(1), 275.
11. Dotto, T. S., Naveira Garabato, A. C., Bacon, S., Tsamados, M., Holland, P. R., Hooley, J., et al. (2018). Variability of the Ross Gyre, SouthernOcean: Drivers and responses revealed by satellite altimetry. Geophysical Research Letters, 45, 6195–6204.
12. Giglio, D., Lyubchich, V., & Mazloff, M. R. (2018). Estimating oxygen in the Southern Ocean using argo temperature and salinity. Journal of Geophysical Research: Oceans, 123(6), 4280-4297.
13. Haumann, F. A., Moorman, R., Riser, S. C., Smedsrud, L. H., Maksym, T., Wong, A. P., ... & Sarmiento, J. L. (2020). Supercooled Southern Ocean waters. Geophysical Research Letters, 47(20), e2020GL090242.
14. Haumann, F. A., Gruber, N., Münnich, M., Frenger, I., & Kern, S. (2016). Sea-ice transport driving Southern Ocean salinity and its recent trends. Nature, 537(7618), 89-92.
15. Hazel, J. E., & Stewart, A. L. (2019). Are the near-Antarctic easterly winds weakening in response to enhancement of the southern annular mode?. Journal of Climate, 32(6), 1895-1918.

16. King, M. A., Lyu, K., & Zhang, X. (2023). Climate variability a key driver of recent Antarctic ice-mass change. Nature Geoscience, 1-8.
17. Klatt, O., Boebel, O., & Fahrbach, E. (2007). A profiling float's sense of ice. Journal of Atmospheric and Oceanic Technology, 24(7), 1301-1308.
18. Locarnini, R. A., O. K. Baranova, A. V. Mishonov, T. P. Boyer, J. R. Reagan, D. Dukhovskoy, D. Seidov, H. E. Garcia, C. Bouchard, S. Cross, C. R. Paver, and Z. Wang, 2023. World Ocean Atlas 2023, Volume 1: Temperature. A. Mishonov Technical Ed. NOAA Atlas NESDIS (in preparation).
19. McMahon, C. R., Roquet, F., Baudel, S., Belbeoch, M., Bestley, S., Blight, C., ... & Woodward, B. (2021). Animal borne ocean sensors–AniBOS–An essential component of the global ocean observing system. Frontiers in Marine Science, 8, 751840.
20. Mazloff, M. R., Cornuelle, B. D., Gille, S. T., & Verdy, A. (2018). Correlation lengths for estimating the large-scale carbon and heat content of the Southern Ocean. Journal of Geophysical Research: Oceans, 123(2), 883-901.
21. Mensah, V., & Ohshima, K. I. (2023). A mapping methodology adapted to all polar and subpolar oceans with a stretching/shrinking constraint. Journal of Atmospheric and Oceanic Technology, 40(10), 1241-1261.
22. Naveira Garabato, A. C., Dotto, T. S.,Hooley, J., Bacon, S., Tsamados, M.,Ridout, A., Frajka-Williams, E. E., Herraiz-Borreguero, L., Holland, P. R., Heorton, H. D. B. S. and Meredith, M. P. (2019). Phased response of the subpolar Southern Ocean to changes in circumpolar winds. Geophysical Research Letters, 46, 6024–6033.
23. Neme, J., England, M. H., & McC. Hogg, A. (2022). Projected changes of surface winds over the Antarctic continental margin. Geophysical Research Letters, 49(16), e2022GL098820.
24. Newman, L., Heil, P., Trebilco, R., Katsumata, K., Constable, A., Van Wijk, E., ... & Spreen, G. (2019). Delivering sustained, coordinated, and integrated observations of the Southern Ocean for global impact. Frontiers in Marine Science, 6, 433.
25. Oke, P. R., Rykova, T., Pilo, G. S., & Lovell, J. L. (2022). Estimating Argo float trajectories under ice. Earth and Space Science, 9(7), e2022EA002312.

26. Pauthenet, E., Sallée, J. B., Schmidtko, S., & Nerini, D. (2021). Seasonal variation of the Antarctic Slope Front occurrence and position estimated from an interpolated hydrographic climatology. Journal of Physical Oceanography, 51(5), 1539-1557.
27. Pellichero, V., Sallée, J. B., Schmidtko, S., Roquet, F., & Charrassin, J. B. (2017). The ocean mixed layer under Southern Ocean sea-ice: Seasonal cycle and forcing. Journal of Geophysical Research: Oceans, 122(2), 1608-1633.
28. Pellichero, V., Sallée, J. B., Chapman, C. C., & Downes, S. M. (2018). The southern ocean meridional overturning in the sea-ice sector is driven by freshwater fluxes. Nature communications, 9(1), 1789.
29. Purich, A., & Doddridge, E. W. (2023). Record low Antarctic sea ice coverage indicates a new sea ice state. Communications Earth & Environment, 4(1), 314.
30. Roach, C. J., & Bindoff, N. L. (2023). Developing a New Oxygen Atlas of the World's Oceans Using Data Interpolating Variational Analysis. Journal of Atmospheric and Oceanic Technology, 40(11), 1475-1491.
31. Reagan, J. R., D. Dukhovskoy, D. Seidov, T. P. Boyer, R. A. Locarnini, O. K. Baranova, A. V. Mishonov, H. E. Garcia, C. Bouchard, S. Cross, C. R. Paver, and Z. Wang (2023). World Ocean Atlas 2023, Volume 2: Salinity. A. Mishonov Technical Ed. NOAA Atlas NESDIS (in preparation).
32. Ridgway, K. R., Dunn, J. R., & Wilkin, J. L. (2002). Ocean interpolation by four-dimensional weighted least squares—Application to the waters around Australasia. Journal of atmospheric and oceanic technology, 19(9), 1357-1375.
33. Rintoul, S. R., Speer, K., Sparrow, M., Meredith, M., Hofmann, E., Fahrbach, E., ... & Gladyshev, S. (2010). Southern Ocean Observing System (SOOS): Rationale and strategy for sustained observations of the Southern Ocean. Proceedings of OceanObs '09: Sustained Ocean Observations and Information for Society.
34. Roquet, F., Guinet, C., Charrassin, J.-B., Costa, D. P., Kovacs, K. M., Lydersen, C., Bornemann, H., Bester, M. N., Muelbert, M. C., Hindell, M. A., McMahon, C. R., Harcourt, R., Boehme, L., & Fedak, M. A. (2021). MEOP-CTD in-situ data collection: A Southern ocean Marine-mammals calibrated sea water temperatures and salinities observations. SEANOE. https://doi.org/10.17882/45461

35. Roemmich, D. and J. Gilson (2009), The 2004-2008 mean and annual cycle of temperature, salinity, and steric height in the global ocean from the Argo Program. Progress in Oceanography, 82, 81-100.
36. Schmidtko, S., Johnson, G. C., & Lyman, J. M. (2013). MIMOC: A global monthly isopycnal upper-ocean climatology with mixed layers. Journal of Geophysical Research: Oceans, 118(4), 1658-1672.
37. Schmidtko, S., Heywood, K. J., Thompson, A. F., & Aoki, S. (2014). Multidecadal warming of Antarctic waters. Science, 346(6214), 1227-1231.
38. Shimada, K., Aoki, S., & Ohshima, K. I. (2017). Creation of a gridded dataset for the southern ocean with a topographic constraint scheme. Journal of Atmospheric and Oceanic Technology, 34(3), 511-532.
39. Siegelman, L., Roquet, F., Mensah, V., Rivière, P., Pauthenet, E., Picard, B., & Guinet, C. (2019). Correction and accuracy of high-and low-resolution CTD data from animal-borne instruments. Journal of Atmospheric and Oceanic Technology, 36(5), 745-760.
40. Sonnewald, M., Reeve, K. A., & Lguensat, R. (2023). A Southern Ocean supergyre as a unifying dynamical framework identified by physics-informed machine learning. Communications Earth & Environment, 4(1), 153.
41. Troupin, C., Barth, A., Sirjacobs, D., Ouberdous, M., Brankart, J. M., Brasseur, P., ... & Beckers, J. M. (2012). Generation of analysis and consistent error fields using the Data Interpolating Variational Analysis (DIVA). Ocean Modelling, 52, 90-101.
42. Verdy, A., & Mazloff, M. R. (2017). A data assimilating model for estimating Southern Ocean biogeochemistry. Journal of Geophysical Research: Oceans, 122(9), 6968-6988.
43. Wilson, E. A., Riser, S. C., Campbell, E. C., & Wong, A. P. (2019). Winter upper-ocean stability and ice–ocean feedbacks in the sea ice–covered Southern Ocean. Journal of Physical Oceanography, 49(4), 1099-1117.
44. Wong, A. P. S., et al. (2020). Argo Data 1999–2019: Two Million Temperature-Salinity Profiles and Subsurface Velocity Observations From a Global Array of Profiling Floats. Frontiers in Marine Science, 7(700). https://doi.org/10.3389/fmars.2020.00700

45. Yamazaki, K., Aoki, S., Shimada, K., Kobayashi, T., & Kitade, Y. (2020). Structure of the subpolar gyre in the Australian-Antarctic Basin derived from Argo floats. Journal of Geophysical Research: Oceans, 125(8), e2019JC015406.
46. Yamazaki, K., Aoki, S., Katsumata, K., Hirano, D., & Nakayama, Y. (2021). Multidecadal poleward shift of the southern boundary of the Antarctic Circumpolar Current off East Antarctica. Science advances, 7(24), eabf8755.

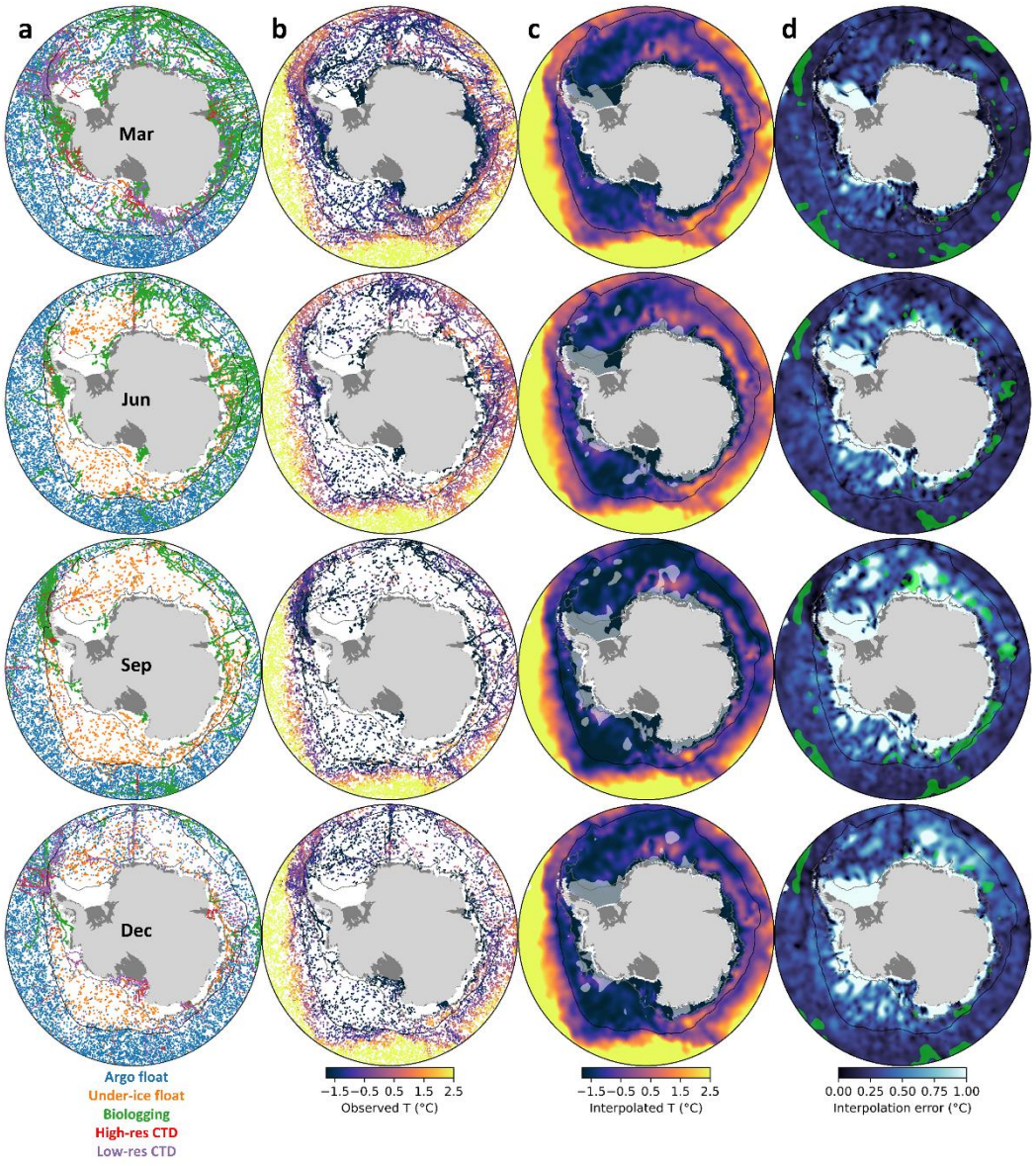

Figure 1. Observations and interpolated fields for March, June, September, and December by row. Columns are: (a) data population colored by platform type. (b) Temperature at 100 m, as measured from in-situ observations. (c) DIVA-interpolated temperature at 100 m; areas with interpolation errors larger than 1°C are masked in gray. (d) Interpolation errors in °C. Standard deviation larger than 1 °C is shown in green. The black line represents the climatological sea ice extent in September, defined by a 15% sea ice concentration (sourced from NSIDC), as the boundary of the seasonal ice zone. The 3,000 m isobath of the continental slope is shown in gray.

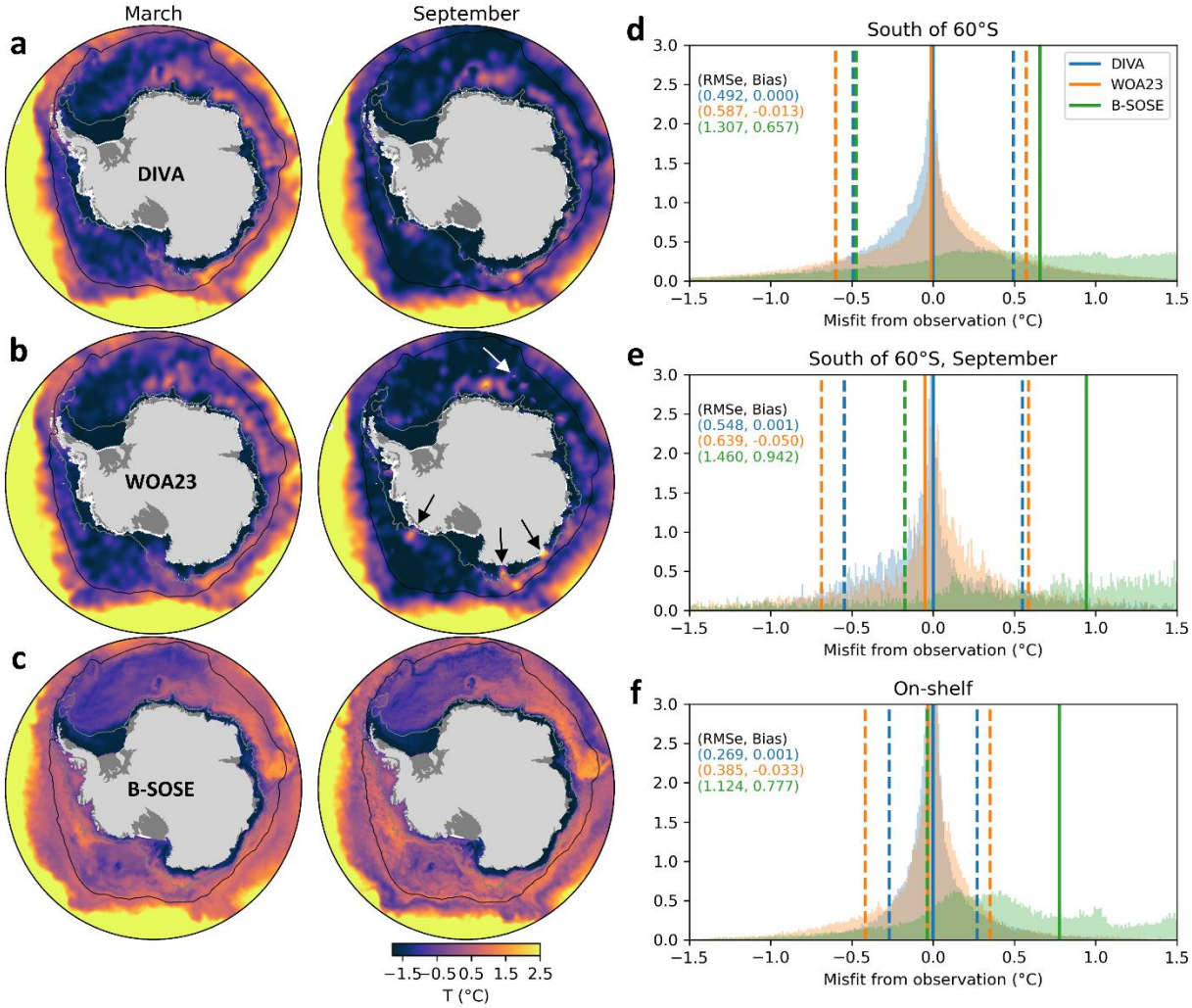

Figure 2. Comparison between three datasets. Monthly-mean temperature at 100 m is shown for (a) DIVA, (b) WOA23, and (c) B-SOSE in March (left) and September (right). In panel (b), spurious features in September are annotated by white and black vectors. (d) Histogram of misfit from observation for 100 m temperature by all available data south of 60°S (blue: DIVA, orange: WOA23, green: B-SOSE). Root-mean-square errors and biases are shown in upper-left figures in the corresponding color and plotted as broken and solid lines, respectively. Data from September (e) and data from the continental shelf defined by sea depths shallower than 1,000 m (f) are also presented. Bin size of histogram is set to 0.01 °C.

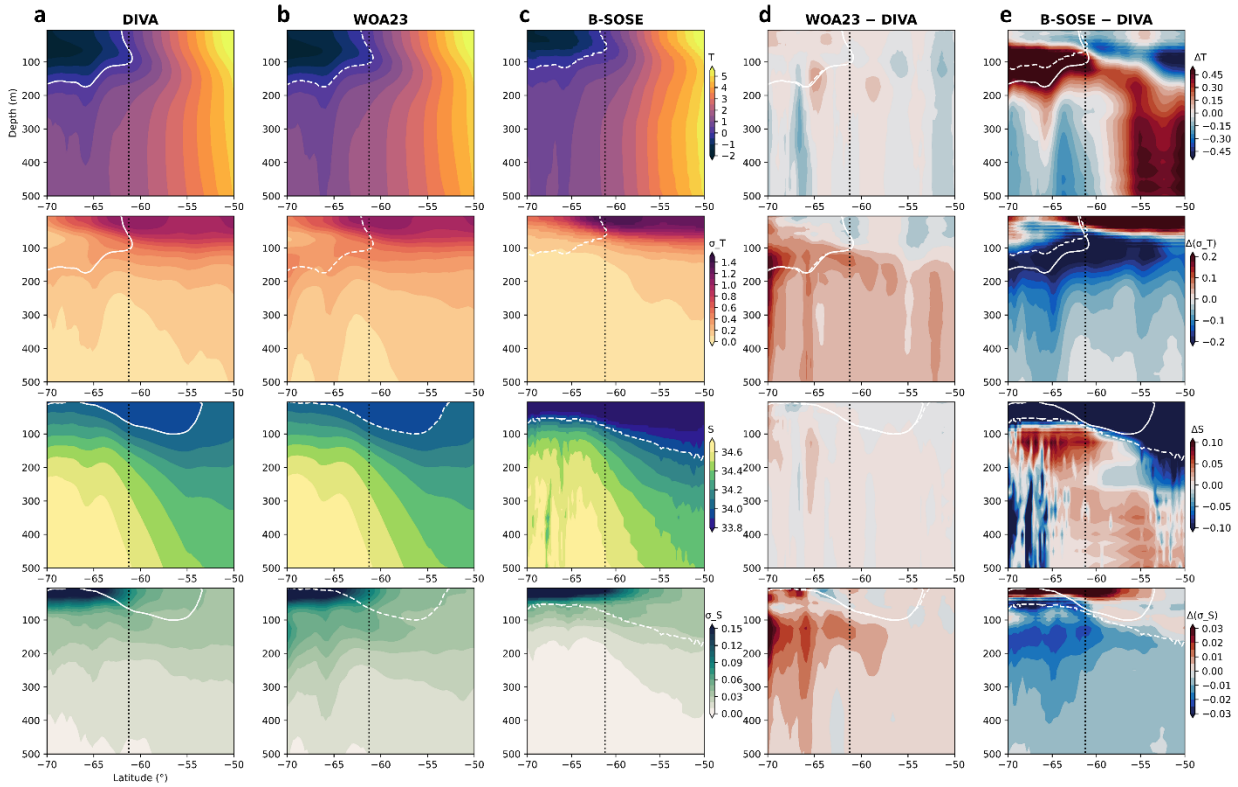

Figure 3. Zonally-averaged meridional sections. The fields displayed by row are: climatological temperature, standard deviation of monthly temperature values (°C), climatological salinity, and standard deviation of monthly salinity values (practical salinity unit), derived from (a) DIVA, (b) WOA23, and (c) B-SOSE. Differences between DIVA and WOA23 (d), as well as DIVA and B-SOSE (e), are also shown. White contour denotes the 0°C isotherm and 34.00 isohaline for DIVA (solid line) and for WOA23 and B-SOSE (dashed line). A vertical dotted line corresponds to the mean latitude of the sea ice extent in September.

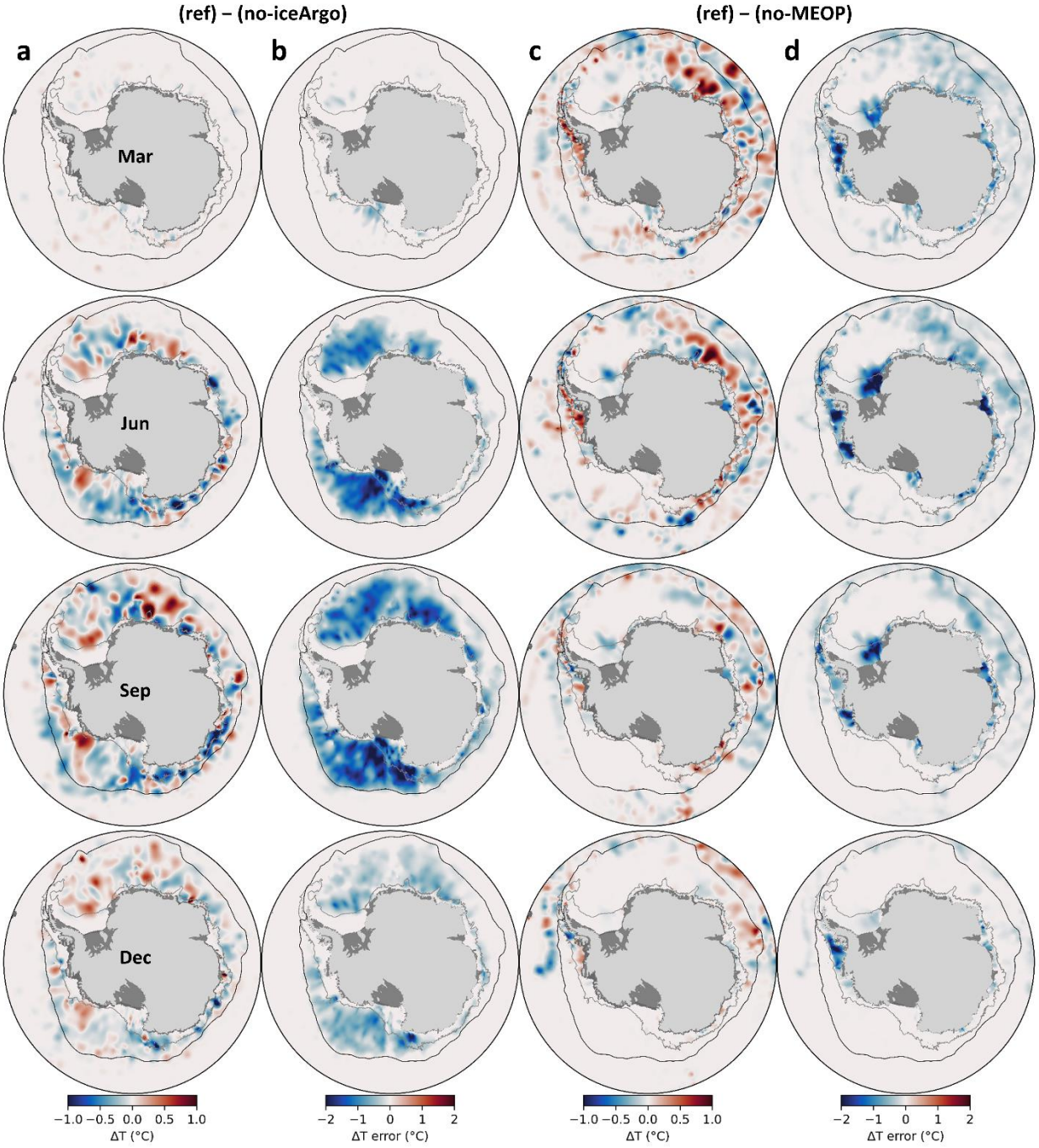

Figure 4. Impact of the under-ice observations. Monthly difference between the reference climatology and the "no-iceArgo" climatology is shown for (a) temperature and (b) temperature interpolation error at 100 m, representing the effect of under-ice Argo data. Panels (c) and (d) are those for "no-MEOP", representing the effect of biologging data. The 3,000 m isobath of the continental slope and the climatological sea ice extent in September are shown as in Figure 1.